Thermally responsive morphological changes of layered coordination polymers induced by disordering/ordering of flexible alkyl chains

Kenichiro Omoto, Shota Aoyama, Tomasz Galica, Eiji Nishibori, Shohei Katao, Kazuma Yasuhara, Gwénaël Rapenne

Thermally responsive morphological change of layered coordination polymer induced by disordering/ordering of flexible alkyl chains

Kenichiro Omoto,*[a] Shota Aoyama,[a] Tomasz Galica,[b] Eiji Nishibori,[b] Shohei Katao,[a] Kazuma Yasuhara,[a,c] and Gwénaël Rapenne[a,d]

[a] *Division of Materials Science, Nara Institute of Science and Technology (NAIST), 8916-5 Takayama-cho, Ikoma, 630-0192, Japan. omoto@ms.naist.jp*

[b] *Department of Physics, Faculty of Pure and Applied Sciences, Tsukuba Research Center for Energy Materials Science (TREMS), University of Tsukuba, 1-1-1 Tennodai, Tsukuba, Ibaraki 305-8571, Japan*

[c] *Center for for Digital Green-innovation, Nara Institute of Science and Technology (NAIST), 8916- 5 Takayama-cho, Ikoma, 630-0192, Japan*

[d] *CEMES, Université de Toulouse, CNRS, 29 Rue Marvig, F-31055 Toulouse Cedex 4, France*

The search for a method to control structural transformations of layered coordination polymers is highly desirable to modulate their properties and functions. Herein, we report the construction of a novel coordination polymer named Zn**C16** with Zn(II) ions coordinated to isophthalates ligands bearing *n*-hexadecyloxy chain (**C16**$^{2-}$). Its structure consists of a layer-by-layer structure of rigid two-dimensional coordination network and an assembly of alkyl chains as a thermally responsive moiety. Single crystals of Zn**C16** exhibit a thermal crystal-to-crystal phase transition behaviour dominated by disordering/ordering of alkyl chains, which induce expansion and shrinkage of the distance within the rigid 2D coordination networks. Microscopic observation revealed that the thermal phase transition of Zn**C16** induces a significant change in their crystal morphology; a reversible macroscopic elongation/shrinkage of crystal dimension driven by displacement of interlayer distances and an irreversible delamination and polycrystal slippage driven by constraints generated from this phase transition. Our result provides a new direction to modulate dynamic behaviour and related properties and functions of layered coordination polymers where the thermally responsive character of flexible alkyl chains works as an important role to tune interlayer interactions.

Introduction

Coordination polymer crystals are of major interest as solid state materials which have well-defined supramolecular networks consisting of organic ligands and metal ions.[1] Various combinations of these metal ions and organic ligands give rise to a wide family of coordination polymers with 1D to 3D periodic networks, exhibiting functions specific to their structures, such as catalysts,[2] absorbents,[3] and magnetic[4] or optical materials.[5] In particular, layered coordination polymers have been extensively studied owing to the anisotropy of their crystal structures, where a robust 2D coordination network is developed to form stacked layers *via* weak interlayer interactions.[6] One of the most prominent features of layered coordination polymers is the

flexibility of their crystal structures, where rigid layers of 2D coordination networks show displacement as modules to modify their stacking modes and interlayer distances without losing in-plane periodic linkage. The search for a method to control such dynamic nature in layered coordination polymers is highly desirable as it has rendered them variety of useful properties and functions, such as the ability to adsorb molecules *via* gate-opening and intercalation[7] and abilities to modulate their macroscopic shapes (morphology) *via* exfoliation into ultrathin nanosheets.[8] However, most of these changes in crystal structures are found serendipitously and it is still challenging to rationally predict and trigger their structural transformation behaviours. Herein, we envisioned that the incorporation of stimuli-responsive moieties on the surface of a 2D framework, which could control stacking modes and interlayer interactions, would provide important insights into how to rationally trigger the structural transformation of layered coordination polymers.

In this article, we describe the construction of a novel coordination polymer (Zn**C16**) consisting of Zn(II) ions and isophthalates functionalised with long alkyl chains (i.e. *n*-hexadecyloxy chain, **C16**$^{2-}$) in a 2D network as a thermally responsive interlayer junction. Molecules with long alkyl chains are known to create soft assembled structures *via* weak intermolecular interactions, such as gel,[9] liquid crystal,[10] and lipid membranes,[11] in which they orientate and packed together. Such condensed assemblies exhibit a thermal phase transition behaviour originated in conformational disordering and ordering (namely melting and crystallisation) of alkyl chains which significantly influence their molecular packing to modify morphology and softness. We envisioned that layered hybridisation of such flexible assemblies of alkyl chains with rigid 2D coordination polymers will enable thermally responsive changes in crystal morphology involving displacement of the rigid metal-organic skeleton affected by loosening and tightening of interlayer interactions.[12]

Zn**C16** also exhibits a crystal-to-crystal thermal phase transition accompanied by disordering/ordering of the flexible long alkyl chains. Detailed microscopic observation revealed that the thermal phase transition of Zn**C16** induces a mechanical crystal response of crystals to modulate their morphology (shape changes and delamination) without a loss of in-plane periodic linkage.[13]

Result and discussion

Preparation of the coordination polymer

As a starting material of a coordination polymer, we selected the *n*-hexadecyloxy substituted isophthalic acid (H_2**C16**). Although H_2**C16** has been used as components of various supramolecular and metal-organic materials, there are no examples of the construction of crystalline coordination polymers with this ligand.[14] As a metal ion, we selected Zn(II) which is widely used as kinetically labile and thermodynamicaly stable coordination centre to create variety of coordination polymers.[15] Single crystals of coordination polymer Zn**C16** were prepared solvothermally by reacting the *n*-hexadecyloxy substituted isophthalic acid (H_2**C16**) with zinc acetate ($Zn(OAc)_2{\cdot}2H_2O$) in methanol at 60 °C (Fig. 1a). The reaction was monitored by powder X-Ray diffraction (PXRD) measurement (Fig. S1). Upon mixing an equimolar amount of H_2**C16** and

$Zn(OAc)_2{\cdot}2H_2O$, a colourless solid formed immediately. Upon heating the resulting solid in methanol at 60 °C for 2 days, the sample gradually turned into plate single crystals of solvated coordination polymer Zn**C16**$(MeOH)_2$ consisting of a 1D polymeric structure with solvated Zn(II) ion as a precursor for Zn**C16** (Fig. S2–4). After further incubation of the solid samples in methanol at 60 °C for another 5 days, Zn**C16** was obtained as colourless prismatic single crystals, the phase purity of which was confirmed by elemental analysis, visual observation using an optical microscope, and X-ray structural analysis (*vide infra*) (Fig. S5–7).

Phase transition behaviour of the coordination polymer

First, the thermal phase transition behaviour of Zn**C16** was studied using thermogravimetric analysis (TGA) and differential thermal analysis (DTA) (Fig. S8). Upon heating single crystals of Zn**C16** starting from room temperature in dried air, no significant weight loss nor a sharp change of heat flow was observed until the temperature approached 150 °C. Upon further heating the sample, a prominent endothermic peak appeared at 153 °C without showing a significant weight loss. This result suggests that Zn**C16** shows a thermal phase transition around 150 °C. Single crystal X-ray diffraction (SCXRD) analysis at two representative temperatures (20 °C and 177 °C) clarified the existence of two different structures; a lower temperature phase (hereafter denoted as **LT**, Fig. 1b–c) and that of a higher temperature phase (hereafter denoted as **HT**, Fig. 1d). In consequence, Zn**C16** exhibits a crystal-to-crystal phase transition at around 150 °C.

In the crystal structure of **LT** at 20 °C, all carboxylic oxygen atoms of $\mathbf{C16}^{2-}$ are coordinated by crystallographically equivalent Zn(II) ions (Fig. 1b and S6). Each Zn(II) ion is bound to carboxylic oxygen atoms of four isophthalates to form a tetrahedral coordination geometry around the metal centre, creating a 2D infinite coordination network developed in parallel to the (001) plane. Both surfaces of the resulting 2D coordination network are functionalised with alkyl chains of the $\mathbf{C16}^{2-}$ in a well-defined *all-trans* configuration (Fig. 1c and S7). The 2D coordination networks stack in the [001] direction with interlayer distances of 19.783 Å, in which alkyl chains of both surfaces interdigitate each other, thus creating an alternate layer-by-layer structure of the 2D coordination networks and alkyl assemblies.

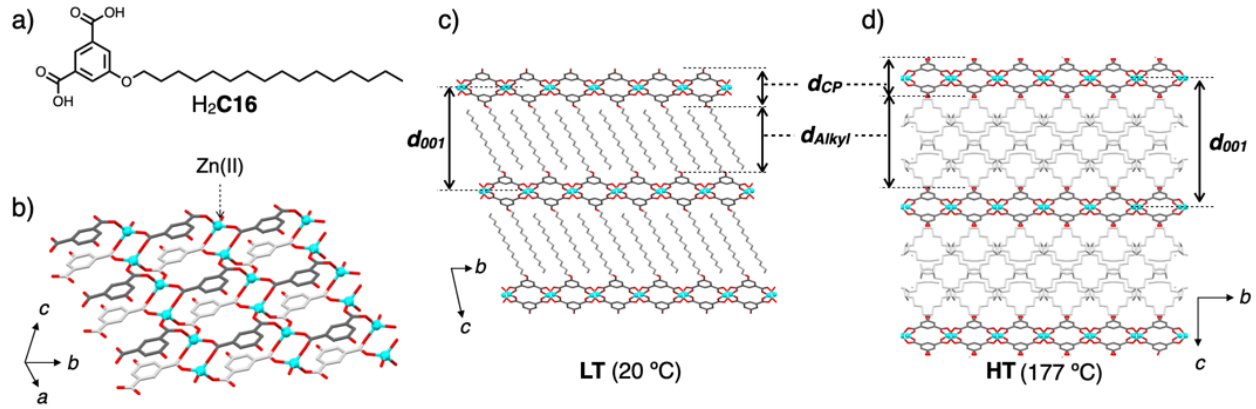

Fig. 1 a) Molecular structure of H_2**C16**. Crystal structures of coordination polymer Zn**C16**; b) structure of 2D coordination polymer network (20 °C, **LT**). Alkyl chains are omitted for clarity. Packing structures

viewed along the *a*-axis of c) **LT** at 20 °C and d) **HT** at 177 °C respectively. Atoms of *n*-hexadecyloxy chains of each **C16**$^{2-}$ in **HT** (Fig. 1d) are disordered over two sites with 50% occupancy (C: gray or dark gray, O: red, Zn: pale blue)

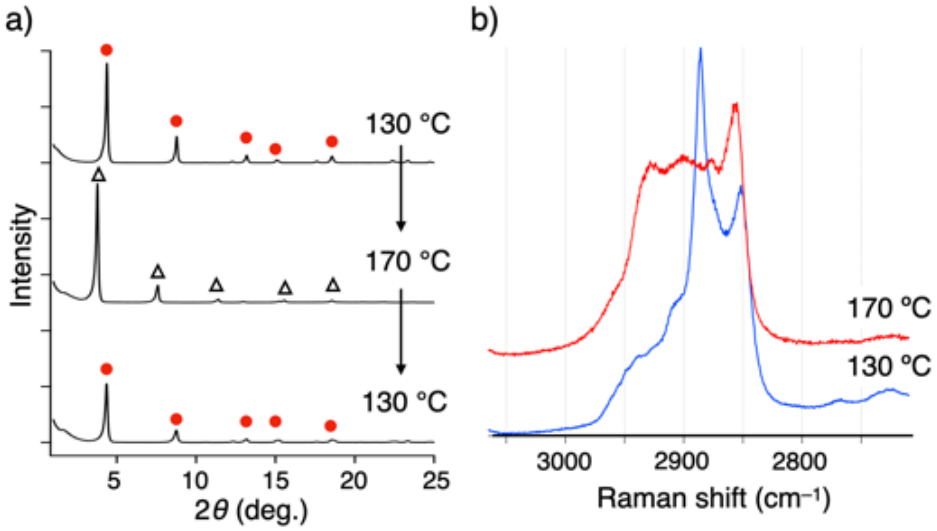

Fig. 2 a) VT-PXRD profiles (λ = 1.54 Å) of Zn**C16** measured sequentially at 130 °C, 170 °C and back to 130 °C. The peaks marked by red circles and black triangles are assignable to the diffraction of **LT** and **HT** respectively. b) Raman spectra (λ_{ex} = 532 nm) of Zn**C16** measured at 130 °C (blue) and 170 °C (red).

The structure of the higher temperature phase **HT** can be obtained by heating the crystals of **LT** as revealed by VT-PXRD in the temperature range of 27–187 °C (Fig. 2a and S9). At room temperature (27 °C), X-ray diffraction of Zn**C16** shows multiple sharp diffraction peaks which match well with the simulated diffraction patterns of **LT** calculated based on its SCXRD structure (Fig. S9). Identical diffraction patterns were observed when the sample was heated up to 130 °C (below the phase transition temperature of 153 °C) (Fig. 2a). On the other hand, upon heating the sample to a temperature of 170 °C (above the phase transition temperature of 153 °C), the original diffraction corresponding to **LT** was replaced by new diffraction peaks corresponding to **HT** (Fig. 2a). The diffraction of **LT** was recovered upon subsequent cooling of the sample to 130 °C (Fig. 2a). Notably, the transition between **LT** and **HT** was continuously observed during repetitive temperature increasing/decreasing cycles within the 130–170 °C window (Fig. S10). X-ray diffraction peaks of both **LT** and **HT** became broad as the repetitive transition proceeded, suggesting the decrease in crystallinity due to the formation of lattice defects and the increase in the crystal mosaicity during the structural transition. Such modifications of the diffraction patterns upon heating/cooling cycles suggests that Zn**C16** exhibits a crystal-to-crystal phase transition accompanied by segmentation of crystal domains to form **LT** and **HT** at lower and higher temperature phases' structures.

The crystal structure of **HT** was resolved using SCXRD analysis of Zn**C16** at 177 °C and then, compared with that obtained for **LT** (Fig. 1d). The temperature-induced phase transition changed

the space group of the crystals from *P*-1 for **LT** to *C*2/m for **HT**. In the obtained structure of **HT**, the electron densities of Zn(II) ions and isophthalate head groups (aromatic rings and carboxylates of $\mathbf{C16}^{2-}$) were clearly observed. Although the thermal factors of these atoms of **HT** are larger than those of **LT**, atom arrangements in the 2D coordination network in both structures are almost the same, where 2D infinite coordination networks consisting of isophthalate head groups coordinated to Zn(II) ions with tetrahedral coordination geometries are formed and stacking in the [001] directions (Fig. 1b–d and S11–12). On the other hand, alkyl chains bound to the 2D coordination network of **HT** are highly disordered and electron density corresponding to the *n*-$C_{16}H_{33}$ chains became blurred, rendering the refinement of atomic coordinates difficult. Therefore, the structure of the *n*-$C_{16}H_{33}$ chains in **HT** was defined as a rigid body fragment based on the blurred electron density, which shows an *all-trans* conformation with a significantly larger thermal factor than that of **LT** (Fig. 1d and S11). Such blurred electron density distribution and large thermal factors of long alkyl chains of **HT** suggests the *n*-$C_{16}H_{33}$ alkyl chains of **HT** are less ordered and exist as a mixture of dynamically and statically disordered domains due to the thermal fluctuation. Although there have been several reports on the construction of coordination polymers with benzene carboxylate-type ligands having long alkyl chains as building blocks,[13bc] the structures of **LT** and **HT** are the first examples to reveal a temperature-dependent disordering/ordering of long alkyl chains based on SCXRD.

Next, we compared the layer-by-layer stacking modes in each crystal structure (**LT** and **HT**). Viewing along the [001] direction, the 2D coordination network of **LT** stacks in a slipped-stacking and shifted manner (Fig. 1c and S7). On the contrary, the 2D coordination network of **HT** stacks in a cofacial-stacking manner with all adjacent structures overlapping each other (Fig. 1d and S11). Interlayer distances between the coordination networks (d_{001}) of **HT** was estimated to be 23.31 Å, which is about 18% larger than that measured in the **LT** phase (19.783 Å). To clarify the origin of such a significant difference in the interlayer distances between **LT** and **HT**, we estimated the thicknesses of the coordination network layer (d_{CP}), alkyl assembly layer (d_{Alkyl}), and (001) planes (d_{001}) of each structure as well as the absolute values of their differentials ($|\Delta|$) from single crystal structures, where $d_{001} = d_{CP} + d_{Alkyl}$ (Fig. 1c–d and Table 1). $|\Delta d_{CP}|$ was found to be less than 0.1 Å, whereas $|\Delta d_{Alkyl}|$ was as large as 3.63 Å, which is comparable to the value of $|\Delta d_{001}|$ (3.53 Å). Such a large contribution of $|\Delta d_{Alkyl}|$ to $|\Delta d_{001}|$ implies that the thermal phase transition between lower and higher temperature phases is driven by the thermal structural transformation of the flexible alkyl chains.

Significant contrast in the fluctuation level of flexible alkyl chains between **LT** and **HT** induces an increase/decrease of their occupied volume in crystals during a thermal phase transition resulting in expansion/shrinkage of the interlayer distance (d_{001}) without breaking the structure of the rigid coordination network. Thus, alkyl chains work as thermally responsive moiety in this layered coordination polymer. Of note, the tilting angle between the *n*-$C_{16}H_{33}$ chains against the (001) plane of **HT** (ca. 40°) was more obtuse than that of **LT** (ca. 37°), which may affect the interlayer displacement of the 2D coordination network along the (001) plane.

Table 1. Comparison of the interlayer distances between **LT** (at 20 °C) and **HT** (at 177 °C) evaluated from their crystal structures (Fig. 1c–d).

Distance	**LT** (Å)	**HT** (Å)	$\|\Delta\|^{d}$
$\boldsymbol{d}_{\mathbf{CP}}$ [a]	7.00	6.91	0.09
$\boldsymbol{d}_{\mathbf{Alkyl}}$ [b]	12.78	16.41	3.63
$\boldsymbol{d}_{\mathbf{001}}$ [c]	19.78	23.31	3.53

[a,b] Distances corresponding to the thickness of the layers of coordination polymer and alkyl assembly. [c] Interlayer distance between (001) planes ($d_{001} = d_{Alkyl} + d_{CP}$, Fig. 1c–d). [d] Absolute differential value between distances of **LT** and **HT**.

The difference in the degree of alkyl chain disorder between **LT** and **HT** was also evaluated based on the Raman spectra of Zn**C16**. The spectrum measured at 130 °C (below phase transition temperature) shows the characteristic band assignable to the vibrations of the symmetric and antisymmetric C–H at 2850 cm^{-1} and 2890 cm^{-1}, respectively (Fig. 2b). In contrast, a band assignable to the C–H stretch is significantly broadened at 170 °C (above the phase transition temperature), as typically observed in the spectra of the alkanes and lipid bilayer above the melting temperature.[16]

Mechanistic investigation

The morphological change of crystals during the transition between **LT** and **HT** can be followed visually using a temperature-controlled optical microscope, revealing that the transition induces a shape change and delamination of single crystals (Movie S1). The face indexing of the prismatic single crystal of **LT** was performed based on SCXRD (Fig. S13). Looking in the [010] direction, as prepared samples of **LT** phase were observed as prismatic crystals of parallelogram shape with (001) and (11-1) faces as an axis whose acute angles were found to be ca. 60° (Fig. 3a). Upon heating the single crystals of **LT** from room temperature up to 150 °C, they remain intact. When the temperature increased to more than 153 °C, the crystal abruptly expanded in the [001] direction (Fig. 3b). Moreover, upon subsequent reduction of the temperature below 150 °C, the shrinkage of the crystals in the [001] direction was observed accompanied by delamination described in the following paragraph (Fig. 3c). The range of temperatures where the shrinkage and elongation of the crystals were visually observed is consistent with the phase transition temperatures evaluated from TGA/DTA and VT-PXRD analysis, suggesting a shape change of the crystals induced by a crystal-to-crystal thermal phase transition. The amplitude of the crystal elongation in the [001] direction was estimated to be about 13% compared to the original length of **LT** before the elongation (Fig 3a–c and S14–15) by measuring the distances between the opposite (001) axis of the parallelogram shape in microscopic images. This expansion coefficient value is comparable to the differential ratio of d_{001} between **LT** and **HT**,

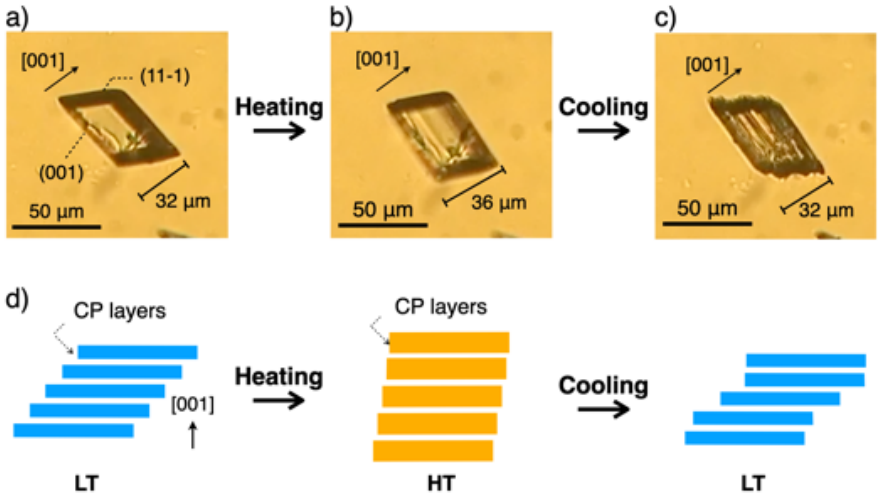

Fig. 3 a-c) Microscopic images on a variable-temperature stage illustrating crystal-to-crystal deformation of Zn**C16** (Movie S1). Heating from 140 °C to 160 °C (a to b) and cooling from 160 °C to 140 °C at 20 °C/min (b to c). d) Schematic representation of the thermally induced morphological change of crystals originating from a combination of reversible extension/shrinkage of layer thickness in the [001] direction and irreversible delamination and polycrystal slippage along the (001) plane. The blue and yellow coloured bars represent cross sectional views of coordination polymer layers of **LT** and **HT** respectively.

suggesting that the observed macroscopic elongation of the crystals in the [001] direction originated in the extension of the interlayer distances of the coordination polymers upon thermal phase transition (Table 1). This thermally-induced crystal elongation/shrinkage in the [001] direction can be performed for continuous cycles of temperature scans even after the formation of the polycrystalline stacked structure by delamination as shown below (Fig. S14–15).

Besides elongation/shrinkage in the [001] direction, the thermal phase transition of crystals induces irreversible delamination along the (001) plane. The slippage among delaminated crystals occurred during the transition to provide staking of displaced polycrystals (typical examples in Fig. 3c). The delamination seemed to occur preferentially during the cooling process rather than in the heating. Scanning electron microscope (SEM) images have been recorded for the **LT** before and after the phase transition, with one cycle of heating and cooling in the 30–170 °C temperature range (Fig. 4). Single crystals of **LT** before the phase transition were observed as a prismatic object with smooth surfaces without remarkable cracks (Fig. 4a). On the other hand, the samples that underwent one cycle of thermal phase transition were observed as stacked polycrystals, in which sheet-like domains 10^1–10^2 nm thick were slipped-stacked parallel to the (001) plane of the initial crystal (Fig. 4b). These results suggest that the phase transition causes delamination of the crystals selectively in the direction parallel to the 2D coordination network staking via weak interlayer interactions.

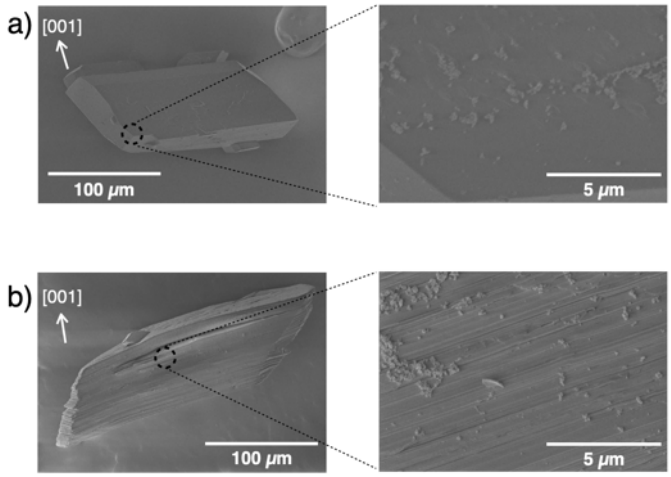

Fig. 4 SEM images of Zn**C16** (**LT**) a) before and b) after one cycle of heating and cooling in the 30–170 °C temperature range. Images of a zoomed region are shown on the right.

To discuss the mechanism of crystal delamination, differential scanning calorimetry (DSC) measurements with multiple heating and cooling cycles were performed (Fig. S16). Upon increasing the temperature of **LT** from 130 to 170 °C, a sharp endothermic peak appeared at 153 °C in the first heating scan. In the following cooling scan, a broad exothermic peak appeared at 148 °C. These peaks correspond to the transition between **LT** and **HT**. As the repetitive temperature scan proceeded, lower temperature shifts of ca. 3 °C of both the endo- and exothermic peaks were observed, which converged after 15 cycles (Fig. S16–17). These peak shifts suggest stabilisation of the higher temperature phase relative to the lower temperature phase upon repeated temperature scanning. Considering these results together with the microscopic observation, delamination along the (001) plane of the crystals during the transition from **HT** to **LT** seems to relax the constraints initially accumulated, resulting in the stabilization of **HT**. Of note, the shape of the exothermic peaks after the second scan became sharper compared to those of the first scan as revealed in the increase in the absolute values of van't Hoff enthalpy of the exothermic peaks (Fig. S17). This result suggests delamination of the crystals also reduces the barrier against the transition to increase its cooperativity.

Thus, we conclude that the morphological change of Zn**C16** crystals originates from the combination of the two factors. The first one is the expansion/shrinkage of interlayer distances of the 2D coordination network driven by the changes in the occupied volume of the flexible long alkyl chains. The second factor is the irreversible delamination and polycrystal slippage preferentially occurring along the coordination network driven by the constraints generated from the phase transitions. (Fig. 3d).

Conclusion

We have constructed a layered coordination polymer Zn**C16** featuring robust 2D coordination networks stacked together *via* soft assembled structures of flexible alkyl chains as thermally responsive moieties. Single crystals of Zn**C16** exhibited a crystal-to-crystal thermal phase

transition driven by disordering/ordering of long alkyl chains that induce expansion/shrinkage of interlayer distances of the 2D coordination network. Detailed microscopic observation revealed that the morphology significantly changed and reversible elongation/shrinkage and irreversible delamination of crystals occurred, where the 2D coordination polymer layer works as the smallest structural modules. Thus, the incorporation of thermally responsive moieties as an interlayer junction is an effective approach to trigger the structural transformation of layered coordination polymers and morphological change. Our results provide an important clue to design layered coordination polymers that can exhibit structural transformations to modulate their functions and properties.

Conflicts of interest

There are no conflicts of interest to declare.

Acknowledgements

This work was financially supported in part by a Grant-in-Aid for Young Scientists (No. 21K14478; K.O.), Fostering Joint International Research (B) (No. 19KK0132; E.N.) and Scientific Research on Innovative Area “Soft Crystal” (area 2903, 18H04499 and 20H04656; E.N.), and “Molecular Engine” (area 8006, 18H05419; G.R.), from the Ministry of Education, Culture, Sports, Science, and Technology, Japan. The synchrotron radiation experiments were performed at BL02B1and BL02B2 of SPring-8 (Proposal Nos. 2018B0074, 2019A0066, 2020A0159, and 2020A0068). Dr. Colin Martin is warmly acknowledged for his careful reading and improving of the manuscript.

Notes and references

1 (a) S. Horike, S. Shimomura and S. Kitagawa, *Nat. Chem*., 2009, **1**, 695–704; (b) W. L. Leong and J. J. Vittal, *Chem. Rev.*, 2011, **111**, 688–764; (c) T. R. Cook, Y.-R. Zheng and P. J. Stang, *Chem. Rev.*, 2013, **113**, 734–777; (d) M. J. Van Vleet, T. Weng, X. Li and J. R. Schmidt, *Chem. Rev.*, 2018, **118**, 3681–3721; (e) E. Fernandez-Bartolome, A. Martinez-Martinez, E. Resines-Urien, L. Piñeiro-Lopez and J. S. Costa, *Coord. Chem. Rev.*, 2022, **452**, 214281.

2 (a) J. Lee, O. K. Farha, J. Roberts, K. A. Scheidt, S. T. Nguyen and J. T. Hupp, *Chem. Soc. Rev.*, 2009, **38**, 1450–1459; (b) V. Pascanu, G. G. Miera, A. K. Inge and B. Martín-Matute, *J. Am. Chem. Soc.*, 2019, **141**, 7223–7234; (c) Q. Wang and D. Astruc, *Chem. Rev.*, 2020, **120**, 1438–1511.

3 (a) S. Kitagawa, R. Kitaura and S.-I. Noro, *Angew. Chem. Int. Ed.*, 2004, **26**, 2334–2375; (b) A. G. Slater and A. I. Cooper, *Science*, 2015, **348**, aaa8075; (c) T. Islamoglu, Z. Chen, M. C. Wasson, C. T. Burum K. O. Kirlikovali, U. Afrin, M. R. Mian and O. K. Farha, *Chem. Rev.*, 2020, **120**, 8130–8160.

4 M. K. Javad, A. Sulaiman, M. Yamashita and Z.-Y. Li, *Coord. Chem. Rev.*, 2022, **467**, 214625.

5 (a) Y. Cui, Y. Yue, G. Qian and B. Chen, *Chem. Rev.*, 2012, **112**, 1126–1162; (b) C. Xu, A. Guenet, N. Kyritsakas, J.-M. Planeix and M. W. Hosseini, *Inorg. Chem.*, 2015, **54**, 10429–10439.

6 G. Chakraborty, I.-H. Park, R. Medishetty and J. J. Vittal, *Chem. Rev.*, 2021, **121**, 3751–3891.

7 (a) A. Kondo, H. Noguchi, S. Ohnishi, H. Kajiro, A. Tohdoh, Y. Hattori, W.-C. Xu, H. Tanaka, H. Kanoh and K. Kaneko, *Nano Lett.*, 2006, **6**, 2581–2584; (b) D. Takana, K. Nakagawa, M. Higuchi, S. Horike, Y. Kubota, T. C. Kobayashi, M. Tanaka and Susumu Kitagawa, *Angew. Chem. Int. Ed.*, 2008, **47**, 3914–3918; (c) K. L. Gurunatha and T. K. Maji, *Inorg. Chem.*, 2009, **48**, 10886–10888.

8 (a) Y. Peng, Y. Li, Y. Ban, H. Jin, W. Jiao, X. Liu and W. Yang, *Science*, 2014, **346**, 1356–1359; (b) A. Anhervé, S. Mañas-Valero, M. Clemente-León and E. Coronado, *Chem. Sci.*, 2015, **6**, 4665–4673; (c) X. Wang, C. Chi, K. Zhang, Y. Qian, K. M. Gupta, Z. Kang, J. Jiang and D. Zhao, *Nat. Commun.*, 2017, **8**, 14460; (d) M. Zhao, Y. Huang, Y. Peng, Z. Huang, Q. Ma and H. Zhang, *Chem. Soc. Rev.*, 2018, **47**, 6267–6295; (e) V. K.-M. Au, K. Nakayashiki, H. Huang, S. Suginome, H. Sato and T. Aida, *J. Am. Chem. Soc.*, 2019, **141**, 53–57; (f) L. Feng, K.-Y. Wang, G. S. Day, M. R. Ryder and H.-C. Zhou, *Chem. Rev.*, 2020, **120**, 13087–13133.

9 (a) K. Kuroiwa, T. Shibata, A. Takada, N. Nemoto and N. Kimizuka, *J. Am. Chem. Soc.*, 2004, **126**, 2016–2021; (b) T. Shimizu, W. Ding and N. Kameta, *Chem. Rev.*, 2020, **120**, 2347–2407.

10 (a) M. Sorai and K. Saito, *Chemical Record*, 2003, **3**, 29–39; (b) T. Kato, N. Mizoshita and K. Kishimoto, *Angew. Chem. Int. Ed.*, 2006, **45**, 38–68; (c) G. L. Nealon, R. Greget, C. Dominguez, Z. T. Nagy, D. Guillon, J.-L. Gallani and B. Donnio, *Beilstain J. Org. Chem.*, 2012, **8**, 349–370; (d) N. Seiki, Y. Shoji, T. Kajitani, F. Ishiwari, A. Kosaka, T. Hikima, M. Takata, T. Someya and T. Fukushima, *Science*, 2015, **348**, 1122–1126; (e) R. Akiyoshi, Y. Hirota, D. Kosumi, M. Tsutsumi, M. Nakamura, L. F. Lindoy and S. Hayami, *Chem. Sci.*, 2019, **10**, 5843–5848.

11 (a) J. F. Nagle, *Ann. Rev. Phys. Chem.*, 1980, **31**, 157–195; (b) K. Ariga, Y. Yamauchi, T. Mori and J. P. Hill, *Adv. Mater.*, 2013, **25**, 6477–6512; (c) R. Mezzenga, J. M. Seddon, C. J. Drummond, B. J. Boyd, G. E. Schröder-Truk and L. Sagalowicz, *Adv. Mater.*, 2019, **31**, 1900818.

12 (a) G. F. Needham and R. D. Willett, *J. Phys. Chem.*, 1984, **88**, 674–680; (b) E.-Y. Choi, C. Gao, H.-J. Lee, O.-P. Kwon and S.-H. Lee, *Chem. Commun.*, 2009, 7563–7565; (c) E.-Y. Choi, H.-J. Lee, C. Gao, O.-P. Kwon and S.-H. Lee, *Macromol. Chem. Phys.*, 2010, **211**, 1955–1959; (d) P. Y. S. Su, S. J. Hsu, J. C. W. Tseng, H.-F. Hsu, W.-J. Wang and I. J. B. Lin, *Chem. Eur. J.*, 2016, **22**, 323–330.

13 (a) N. K. Nath, M. K. Panda, S. C. Sahoo and P. Naumov, *CrystEngComm*, 2014, **16**, 1850–1858; (b) P. Naumov, S. Chizhik, M. K. Panda, N. K. Nath and E. Boldyreva, *Chem. Rev.,* 2015, **115**, 12440–12490; (c) P. Commins, I. T. Desta, D. P. Karothu, M. K. Panda and P. Naumov, *Chem. Commun.*, 2016, **52**, 13941–13954; (d) S. Saha, M. K. Mishra, C. M. Reddy and G. R. Desiraju, *Acc. Chem. Res.,* 2018, **51**, 2957−296; (e) F. Lancia, A. Ryabchun and N. Katsonis, *Nat. Rev. Chem.*, 2019, **3**, 536–551; (f) S. K. Park and Y. Diao, *Chem. Soc. Rev.*, 2020, **49**, 8287–8314; (g) P. Naumov, D. P. Karothu, E. Ahmed, L. Catalano, P. Commins, J. M. Halabi, M. B. Al-Handawi and L. Li, *J. Am. Chem. Soc.*, 2020, **142**, 13256–13272.

14 (a) F. M. Menger and S. J. Lee, *J. Am. Chem. Soc.*, 1994, **116**, 5987–5988; (b) P. Reb, K. Margarit-Puri, M. Klapper and K. Müllen, *Macromolecules*, 2000, **33**, 7718–7723; (c) A. S. Klymchenko, S. Furukawa, K. Müllen, M. V. der Auweraer and S. D. Feyter, *Nano Lett.*, 2007, **7**, 791–795; (d) M. Li, M. Zhang, Y. Lai, Y. Liu, C. Halbert, J. F. Browning, D. Liu and P. Yin, *J. Phys. Chem. C*, 2020, **124**, 15656–15662.

15 (a) L. Qiu, C. Yu, X. Wang, Y. Xie, A. M. Kirillov, W. Huang, J. Li, P. Gao, T. Wu, X. Gu, Q. Nie and D. Wu, *Inorg. Chem.*, 2019, **58**, 4524–4533; (b) R. Abazari, E. Yazdani, M. Nadafan, A. M. Kirillov, J. Gao, A. M. Z. Slawin and C. L. Carpenter-Warren, *Inorg. Chem.,* 2021, **60**, 9700–9708; (c) X. Luo, R. Abazari, M. Tahir, W. K. Fan, A. Kumar, T. Kalhorizadeh, A. M. Kirillov, A. R. Amani-Ghadim, J. Chen and Y. Zhou, *Coord. Chem. Rev*., 2022, **461**, 214505.

16 D. F. H. Wallach, S. P. Verma and J. Fookson, *Biochimica et Biophysica Acta*, 1979, **559**, 153–208.

Supporting Information

Thermally responsive morphological change of layered coordination polymer induced by disordering/ordering of flexible alkyl chains

Kenichiro Omoto,*[a] Shota Aoyama,[a] Tomasz Galica,[b] Eiji Nishibori,[b] Shohei Katao,[a] Kazuma Yasuhara,[a,c] and Gwénaël Rapenne[a,d]

[a] *Division of Materials Science, Nara Institute of Science and Technology (NAIST), 8916-5 Takayama-cho, Ikoma, 630-0192, Japan. omoto@ms.naist.jp*

[b] *Department of Physics, Faculty of Pure and Applied Sciences, Tsukuba Research Center for Energy Materials Science (TREMS), University of Tsukuba, 1-1-1 Tennodai, Tsukuba, Ibaraki 305-8571, Japan*

[c] *Center for for Digital Green-innovation, Nara Institute of Science and Technology (NAIST), 8916-5 Takayama-cho, Ikoma, 630-0192, Japan*

[d] *CEMES, Université de Toulouse, CNRS, 29 Rue Marvig, F-31055 Toulouse Cedex 4, France*

1. Abbreviation

DSC: differential scanning calorimetry, DTA: differential thermal analysis, OAc: -$OCOCH_3$, PXRD: powder X-ray diffraction, SEM: scanning electron microscope, SCXRD: single crystal X-ray diffraction, TGA: thermogravimetric analysis, XRD: X-ray diffraction.

2. Materials and methods

Materials

All solvents, organic and inorganic reagents are commercially available and were used without further purification. Organic ligand (H_2**C16**) was prepared according to previously reported procedures.[1]

Single-crystal X-ray crystallographic analysis using MoK*α* radiation

Single crystal X-ray crystallographic analysis was performed using a Rigaku VariMax RAPID（1.2kW）diffractometer with confocal mirror optics MoK*α* radiation. Single crystals for diffraction measurement were mounted with epoxy resin on a glass fiber, the temperature of which was controlled using a nitrogen gas-flow. Crystal structures were solved with SHELXT[2] and L.S refinement was performed with SHELXL[3] within Olex2 GUI.[4] Hydrogen atoms were refined using the riding model.

Single-crystal X-ray crystallographic analysis using synchrotron

Single crystal X-ray diffraction data was collected at SPring-8, BL02B1 with wavelength 0.24792 Å. Data integration, scaling and multi-scan absorption corrections were carried out with CrysAlisPro[5]. For **HT**, all non-hydrogen atoms were refined anisotropically and hydrogen atoms were treated geometrically with HFIX 43, 23 and 133. **HT** required the following restraints and constraints: FLAT, DANG, ISOR, DELU. C_{16}-akyl chain of **HT** was treated as a rigid fragment, with PART-1. Initial orientation of the chain was assigned basing on two positive electron density peaks for atoms C15 and C16.

Powder X-ray diffraction (PXRD) measurements using CuK*α* radiation

PXRD analysis was carried out using a Rigaku SmartLab (9kW, CuK*α*) diffractometer equipped with a HyPix-3000 as a detector. Samples for diffraction measurement were placed on an oriented silicon plate or a glass plate. For the measurement under controlled temperature condition, an Anton Paar DHS 1100 sample stage was used. The sample was covered with a carbon dome and vacuumed during measurements.

Powder X-ray diffraction (PXRD) measurements using synchrotron

Synchrotron PXRD measurements carried out at SPring-8, BL02B2 beam line using a Large Debye Scherrer camera with an imaging plate as a detector. The samples (crystals of Zn**C16)** were installed in a

glass capillary, the temperature of which was controlled using a nitrogen gas-flow high temperature device. An exposure time of X-ray for each profile was 5 min. The CeO2 (NIST SRM674a) standard powder was used for wavelength calibration. The wavelength was 0.78 Å.

Thermogravimetric analysis and differential thermal analysis (TGA/DTA)

TGA/DTA were performed using a Hitachi STA7200 under dried air. Samples (crystals of Zn**C16**) for the measurement were placed in standard aluminum pan and scanned at a heating rate of 1 °C/min in the temperature range of rt to 500 °C.

Differential scanning calorimetry (DSC) measurement

DSC measurements were performed using a Hitachi DSC7000X under N_2 atmosphere. Samples (crystals of Zn**C16**) for the measurement were placed in standard aluminum pan crimped with a cover and scanned at a heating/cooling rate of 1 °C/min in the temperature range of 130 to 170 °C.

Raman spectroscopy

Raman spectrum of the crystals of Zn**C16** were collected using a JACSO NRS-4100-30 spectrometer using laser of 532 nm for excitation. The sample was placed on a glass plate, the temperature of which was controlled using a Linkam 10083L sample stage.

Observation of crystal using optical microscope

Microscopic images of the crystals of Zn**C16** were collected using an Olympus BX51 attached with a Mettler HS82 sample stage.

Observation of crystal using scanning electron microscope (SEM)

SEM images of the crystals of Zn**C16** before/after one cycle of thermal phase transition were collected using a Hitachi SU6600. The samples were attached on a metal plate using conductive tape. Sample after one cycle of phase transition was prepared by heating and cooling the crystals of Zn**C16** in the 30–170 °C temperature range using DSC (heating/cooling rate: 1 °C/min).

3. Preparation of coordination polymer ZnC16

Procedure

5-(*n*-Hexadecyloxy)-isophthalic acid (H_2**C16**) (300.9 mg, 0.74 mmol, 1 eq) was dissolved in hot MeOH (37 mL) to give a colourless solution. To this solution was added a solution of $Zn(OAc)_2 \cdot 2H_2O$ (20 mM, 37 mL, 0.74 mmol, 1eq). After incubating the resulted colourless suspension at 60 °C for 7 days, colourless prismatic single crystals suitable for single crystal X-ray diffraction analysis were formed (During the incubation process, small amount of solid sample was collected and PXRD was measured to monitor the reaction, Fig. S1). To isolate coordination polymer (Zn**C16**), the single crystals were collected by centrifugation and washed by MeOH. After being kept under reduced pressure at room temperature, Zn**C16** (262.0 mg, 0.56 mml, 75%) were obtained as colourless single crystals (Fig. S5).

Elemental analysis: calcd for $C_{25}H_{38}O_4Zn$ (Zn**C16**): C, 61.34; H, 7.72. Found: C, 61.43; H, 7.78.

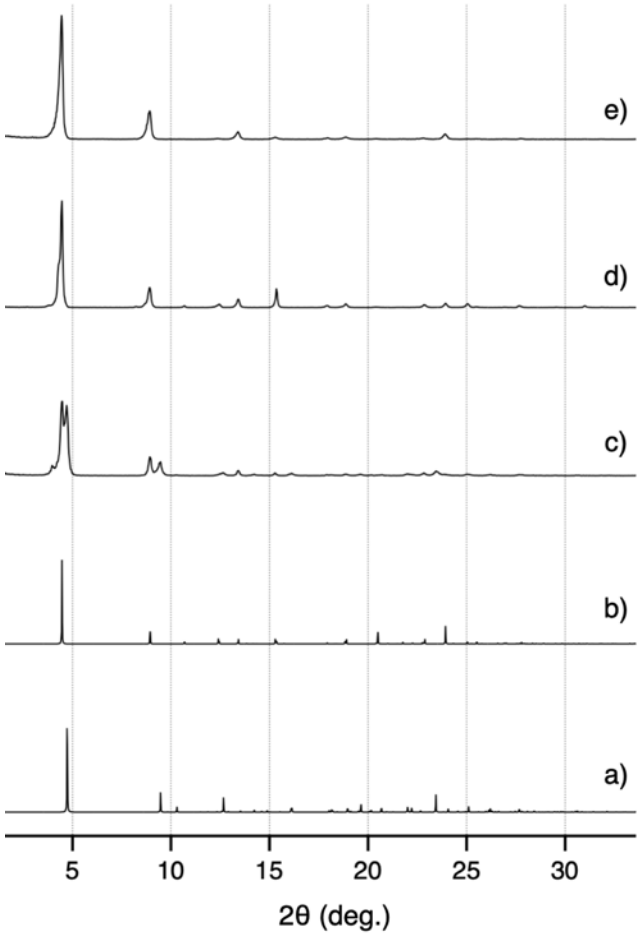

Fig. S1 PXRD profiles of a) Zn**C16** (**LT**) and b) Zn**C16**$(MeOH)_2$ calculated from respective single crystal structures at 20 °C. PXRD profiles (CuKα, λ = 1.541 Å, r.t.) of the a) solid samples formed after incubation of the mixture of H_2**C16** and $Zn(OAc)_2 \cdot 2H_2O$ in MeOH at 60 °C for c) 2 days and d) 7 days. e) PXRD profiles of Zn**C16** (**LT**) isolated as single crystals.

4. Experimental data

4-1. Single crystal structure of solvated coordination polymer ZnC16(MeOH)$_2$

Crystal data for ZnC16(MeOH)$_2$ at 293 K (20 °C)

Crystal data for $C_{26}H_{44}O_7Zn$: Fw = 533.98, crystal dimensions 0.2 × 0.1 × 0.03 mm, triclinic, space group $P\bar{1}$, a = 8.0069(3), b = 9.7526(4), c = 18.8575(9) Å, α = 82.319(6), β = 89.523(6), γ = 68.639(5)°, V = 1357.78(11) Å^3, Z = 2, ρ_{calcd} = 1.306 g·cm^{-3}, μ = 0.945 mm^{-1}, T = 293 K, λ(MoKα) = 0.71075 Å, $2\theta_{max}$ = 55.0°, 6215/4588 reflection collected/unique (R_{int} = 0.0497), R_1 = 0.0488 ($I > 2\sigma(I)$), wR_2 = 0.1262 (for all data), GOF = 1.022, largest diff. peak and hole 0.463/ –0.409 eÅ^{-3}. CCDC deposit number 2201471.

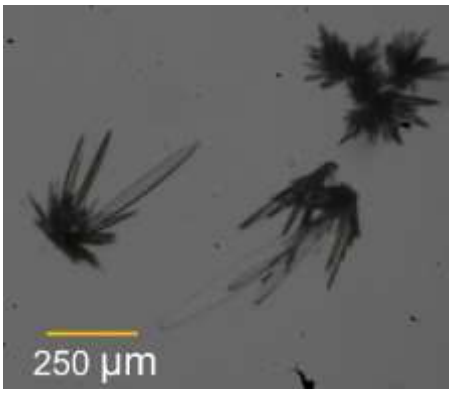

Fig. S2 Microscopic image of Zn**C16**(MeOH)$_2$.

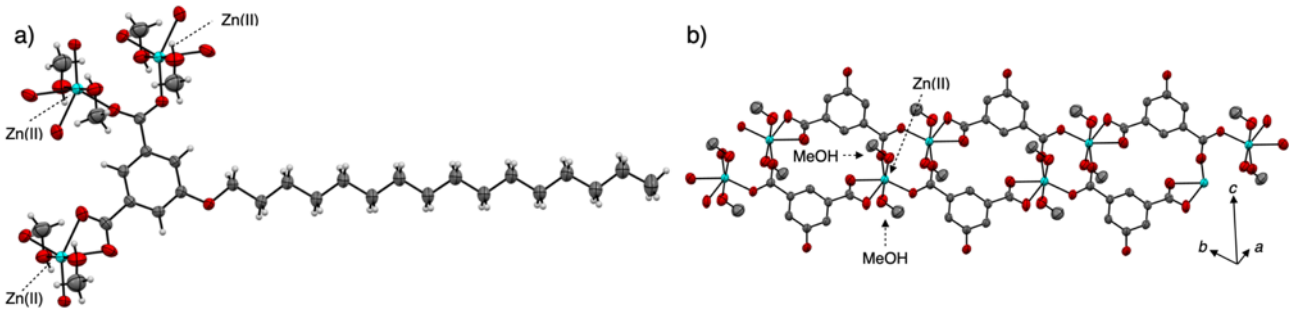

Fig. S3 Crystal structure of Zn**C16**(MeOH)$_2$. a) ORTEP view (50% probability level) of the single ligand. b) Structure of the 1D coordination polymer. Alkyl chains on Fig. S3b are omitted for clarity. (C: grey, H: white, O: red, Zn: pale blue)

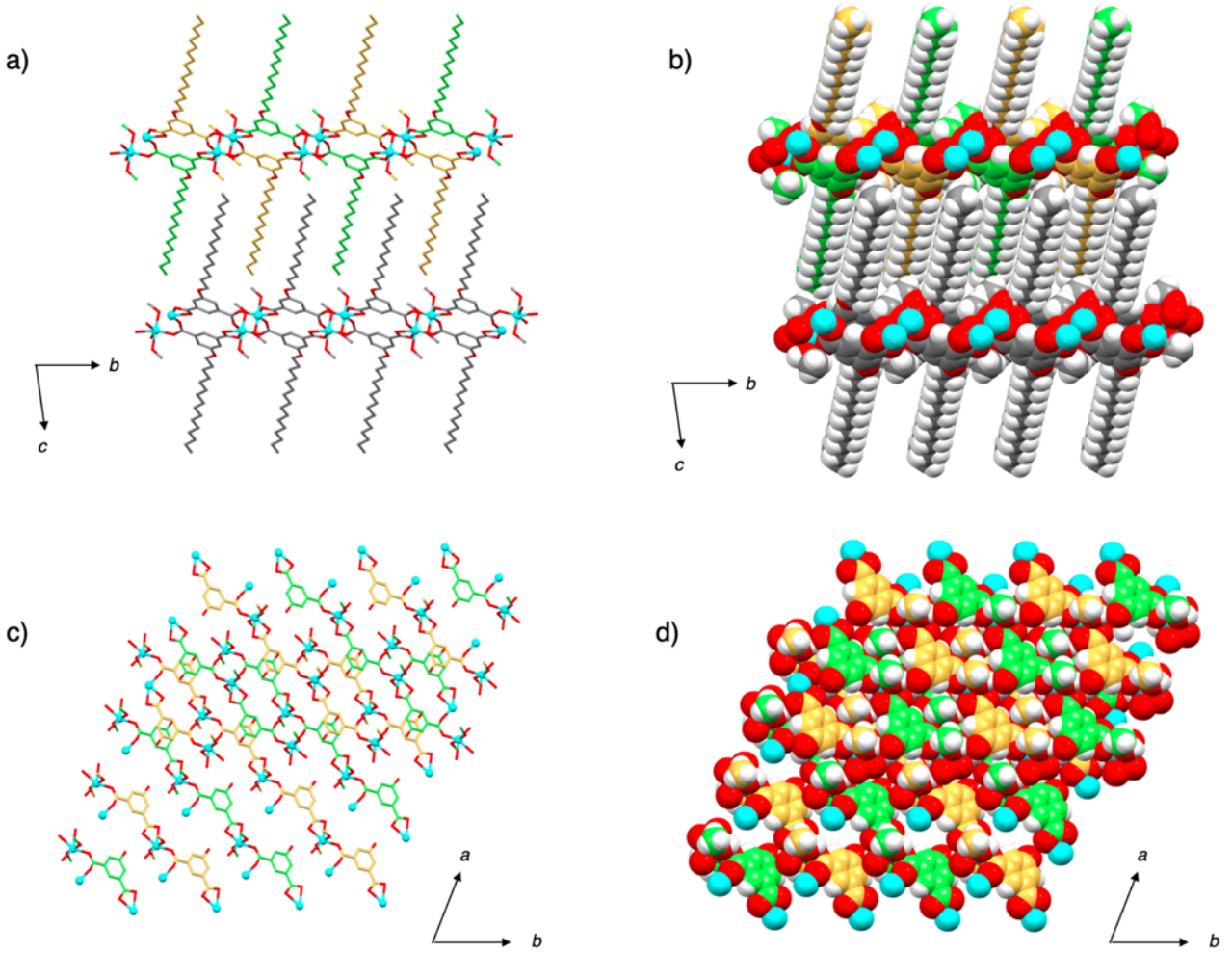

Fig. S4 Molecular packing of Zn**C16**$(MeOH)_2$. Views from *a*-axis with a) ball and stick model and b) space fill model. Views without showing alkyl chains from *c*-axis; c) ball and stick model and d) space fill model. C atoms are shown in different colours for clarity. Alkyl chains on Fig. S4c,d are omitted for clarity. (C: pale green, yellow or grey, H: white, O: red, Zn: pale blue)

4-2. Single crystal structure of coordination polymer ZnC16 (LT)

Crystal data for ZnC16 (LT) at 293 K (20 °C)

Crystal data for $C_{24}H_{36}O_5Zn$: F_w = 469.90, crystal dimensions 0.14 × 0.06 × 0.04 mm, triclinic, space group P–1, a = 7.0651(2), b = 9.0096(3), c = 20.2493(5) Å, α = 78.148(5), β = 89.073(6), γ = 69.912(5)°, V = 1182.65(7) Å^3, Z = 2, ρ_{calcd} = 1.320 gcm^{-3}, μ = 1.069 mm^{-1}, T = 293 K, λ(MoKα) = 0.71075 Å, 2θ_{max} = 55.0°, 5403/4989 reflection collected/unique (R_{int} = 0.0156), R_1 = 0.0266 ($I > 2\sigma(I)$), wR_2 = 0.0715 (for all data), GOF = 1.130, largest diff. peak and hole 0.502/–0.214 eÅ^{-3}. CCDC deposit number 2194401.

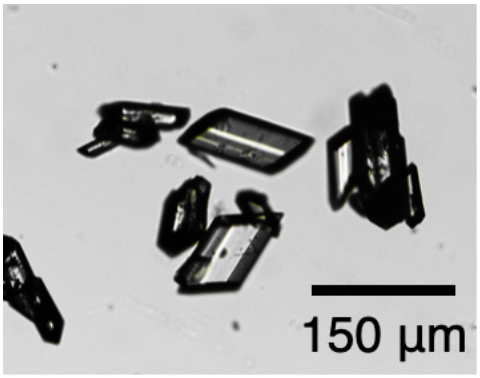

Fig. S5 Microscopic image of Zn**C16** (**LT**) isolated as single crystals.

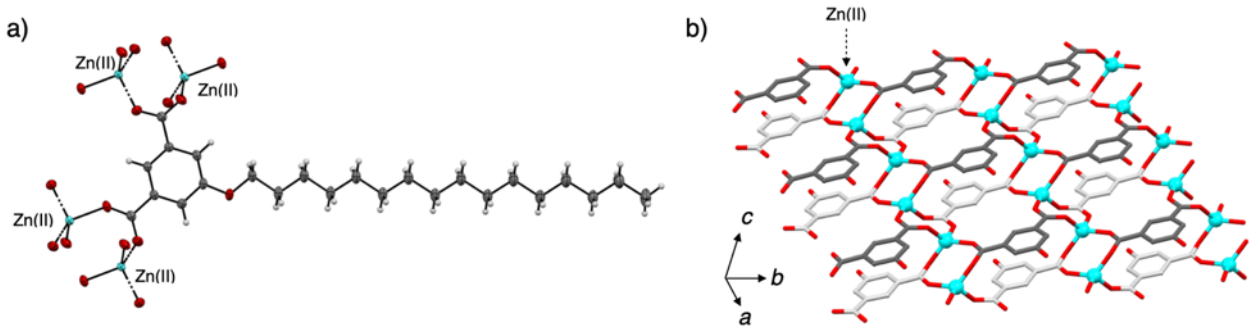

Fig. S6 Crystal structure of Zn**C16** (**LT**). a) ORTEP view (50% probability level) of the single ligand. b) Structure of the 2D coordination polymer network. Alkyl chains on Fig. S6b are omitted for clarity. (C: grey and pale grey, H: white, O: red, Zn: pale blue)

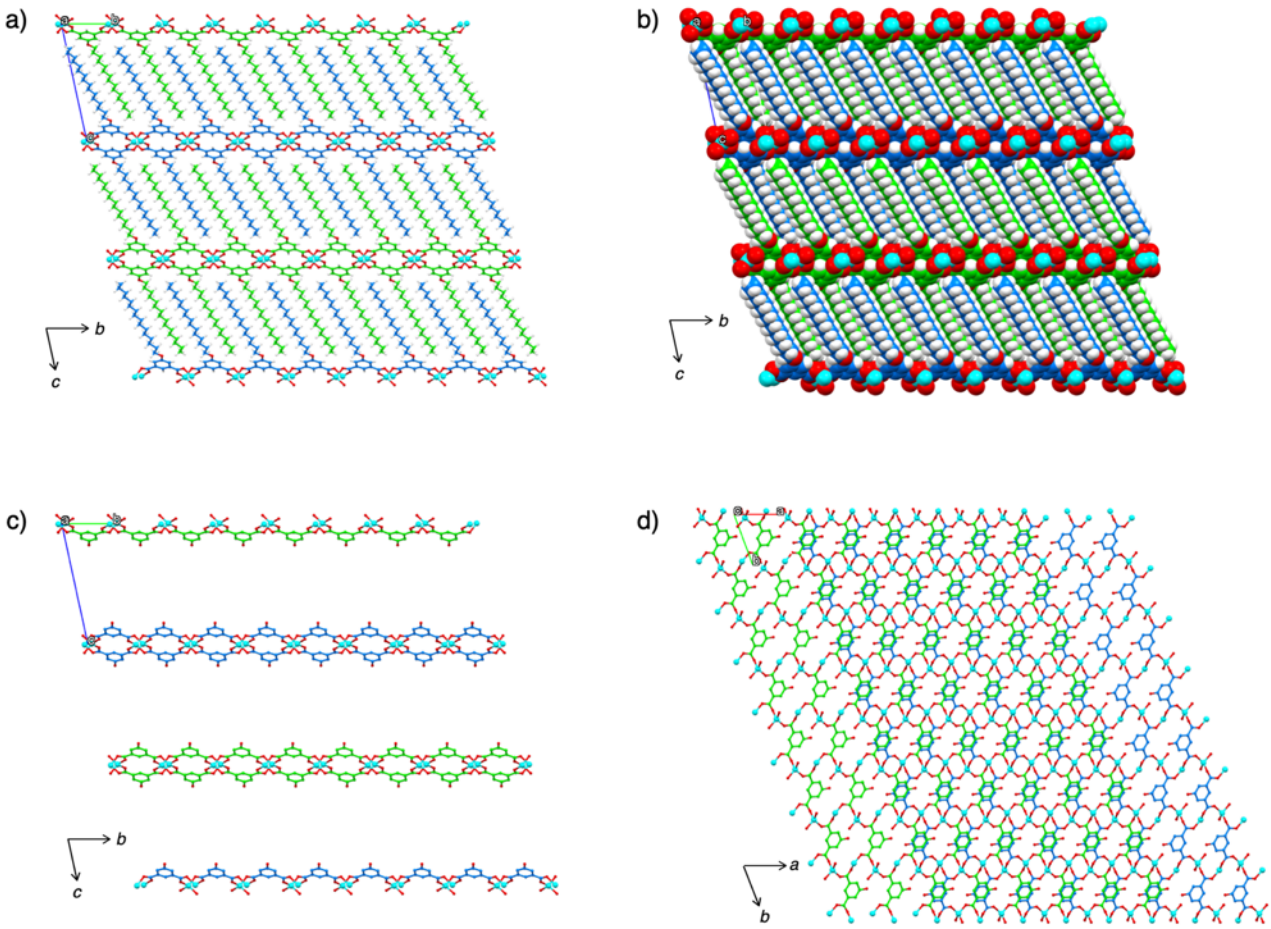

Fig. S7 Molecular packing of Zn**C16** (**LT**). Views from *a*-axis with a) ball and stick model and b) space filling model. Views without showing alkyl chains c) from *a*-axis and d) from *c*-axis. C atoms of the adjacent layer are shown in different colours. Alkyl chains on Fig. S7c,d are omitted for clarity. (C: pale green or blue, H: white, O: red, Zn: pale blue)

4-3. TGA/DTA thermograms of coordination polymer ZnC16

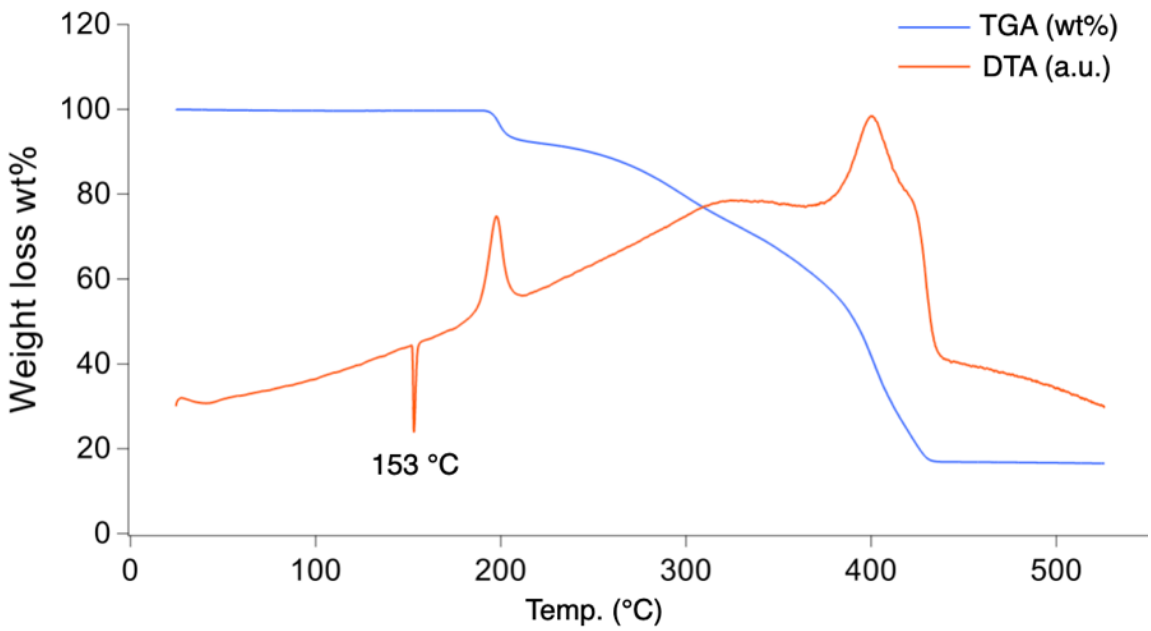

Fig. S8 TGA/DTA thermograms of Zn**C16** measured under dried air (scan rate 1 °C/min).

4-4. Variable temperature PXRD of coordination polymer ZnC16

4-4-1. PXRD of ZnC16 under the temperature window of 27–187 °C

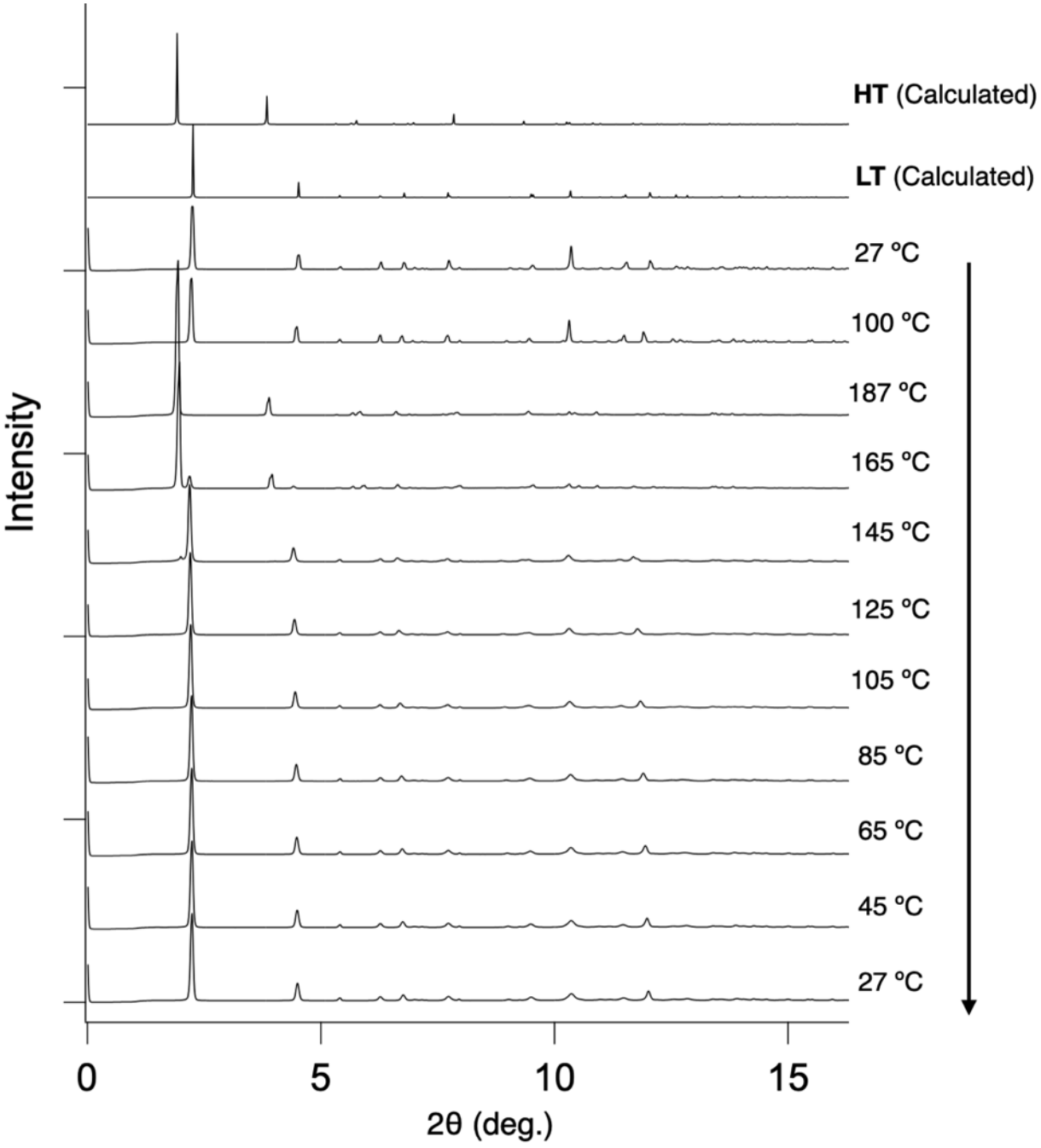

Fig. S9 PXRD profiles (λ = 0.78 Å, synchrotron) of Zn**C16** measured sequentially at 27 °C to 187 °C and back to 27 °C. The theoretical diffraction patterns of **HT** and **LT** are simulated from their single crystal structures at 20 °C and 177 °C respectively. The black arrow shows the order of the measurements.

4-4-2. PXRD of ZnC16 under repetitive heating/cooling scan in the temperature window of 130–170 °C

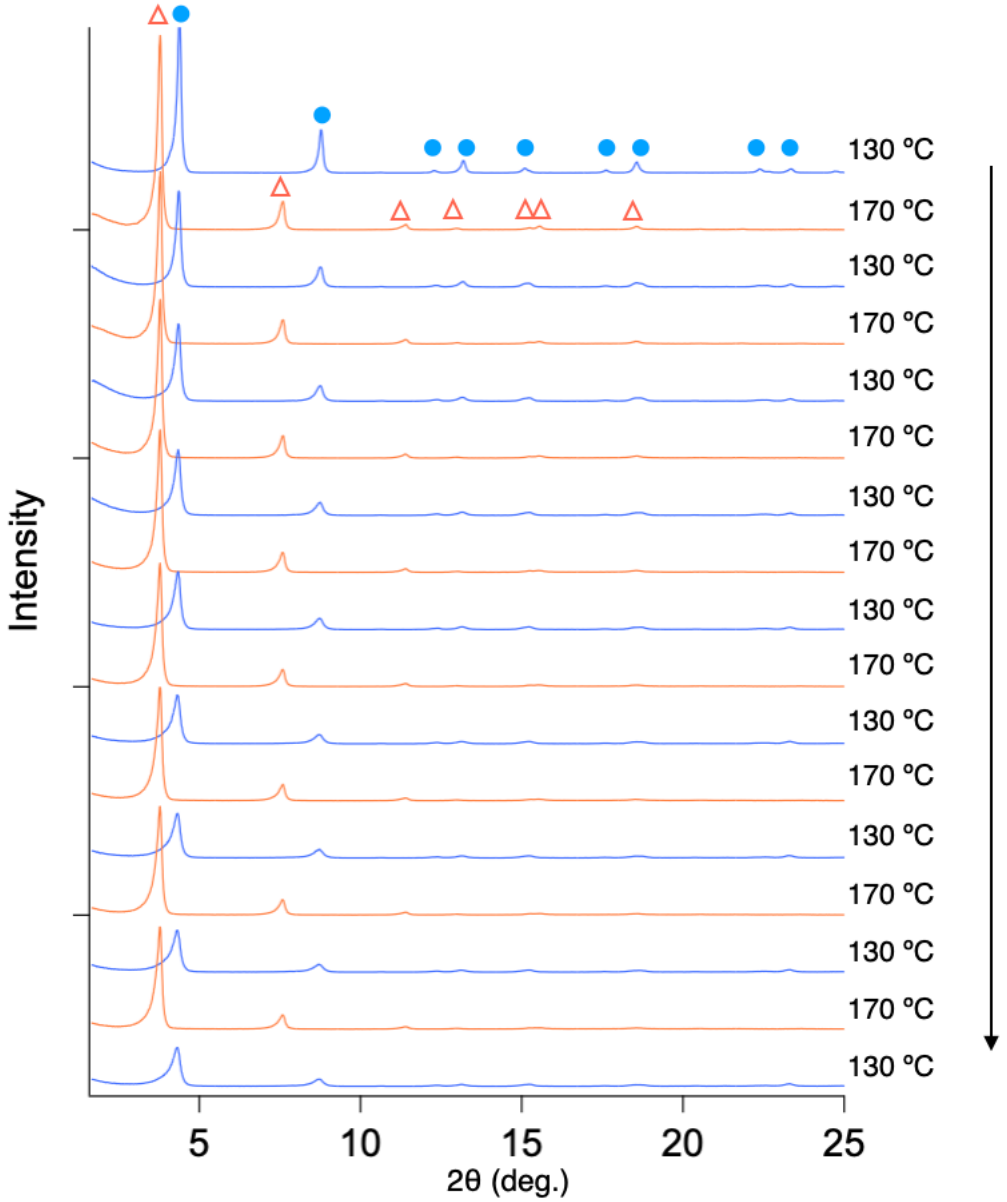

Fig. S10 PXRD profiles (λ = 1.54 Å, CuKα) of Zn**C16** measured during repetitive temperature increasing/decreasing cycles within the 130–170 °C window. The peaks marked by blue circles and red triangles are assignable to the diffraction of **LT** and **HT** respectively. The black arrow shows the order of the measurements.

4-5. Single crystal structure of coordination polymer ZnC16 (HT)

Crystal data for ZnC16 (HT) at 460 K (177 °C)

Crystal data for $C_{24}H_{36}O_5Zn$: F_w = 469.90, crystal dimensions 0.1 × 0.1 × 0.1 mm, monoclinic, space group *C2/m*, a = 7.3454(16), b = 16.8251(13), c = 23.326(14) Å, β = 91.95(4)°, V = 2881.1(19) Å^3, Z = 4, ρ_{calcd} = 1.083 g·cm^{-3}, μ = 0.063 mm^{-1}, T = 450 K, λ(MoKα) = 0.24792 Å, 2θ_{max} = 14.16000°, 3027/913 reflection collected/unique (R_{int} = 0.0977), R_1 = 0.1156 ($I > 2\sigma(I)$), wR_2 = 0.4144 (for all data), GOF = 1.035, largest diff. peak and hole 0.454/-0.230 eÅ^{-3}. CCDC deposit number 2194402.

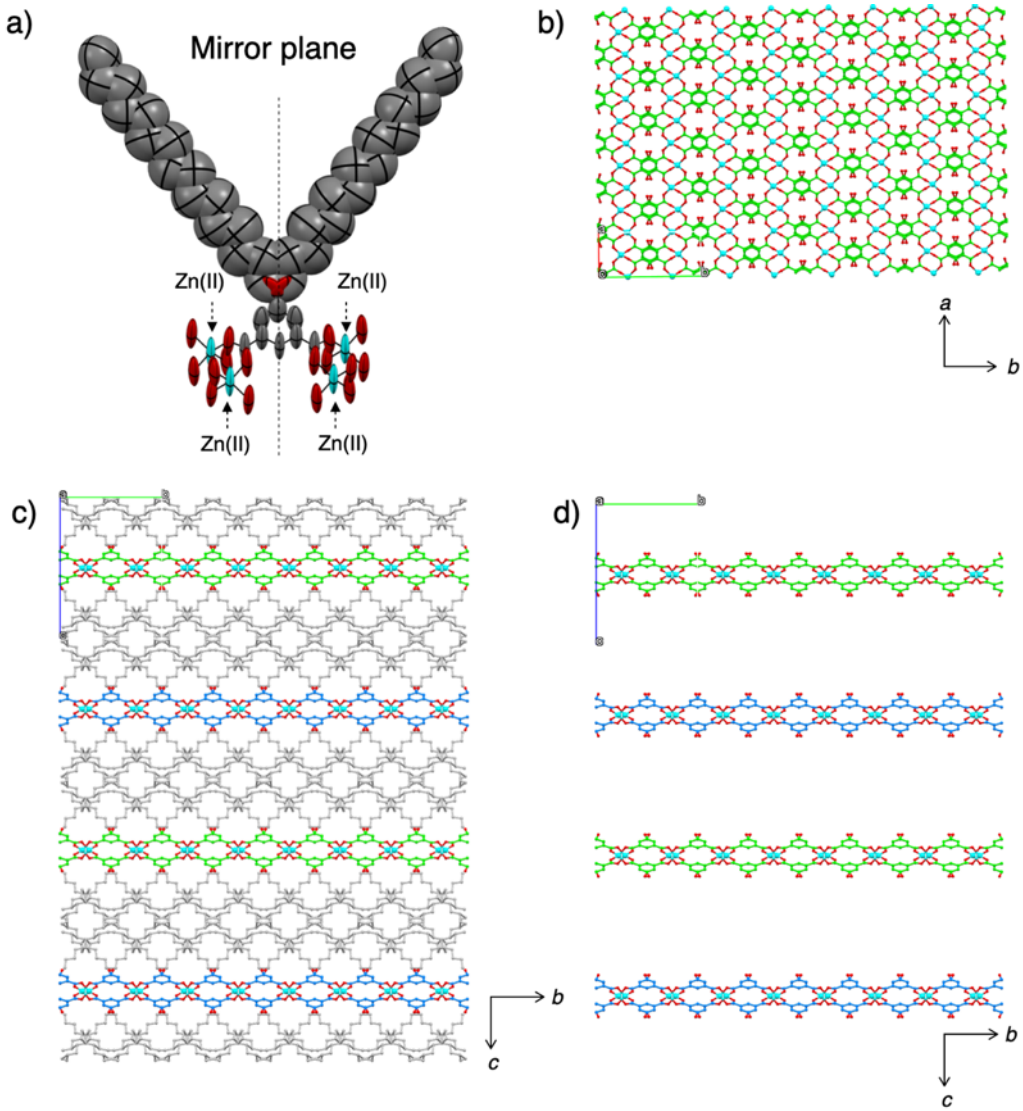

Fig. S11 Crystal structure of Zn**C16** (**HT**) at 177 °C. a) ORTEP view (50% probability level) of single ligand. Structure of 2D coordination polymer network. Views from b) *c*-axis and c,d) from *a*-axis with ball and stick model. C atoms of the aromatic rings of the adjacent layer are shown in different colours. Atoms of *n*-hexadecyloxy chains of each **C16**$^{2-}$ on Fig. S11a,c are disordered over two sites with 50% occupancy. Alkyl chains on Fig. S11b,d are omitted for clarity. (C of the aromatic rings: pale green or blue, C of the alkyl chains: pale gray, O: red, Zn: pale blue)

Table S1. Comparison of the key cell parameters of the single crystal structures of **LT** and **HT**.

	LT (293 K)	**HT (450 K)**
Empirical formula	$C_{24}H_{36}O_5Zn$	$C_{24}H_{36}O_5Zn$
Crystal system	Triclinic	Monoclinic
Space Group	*P*–1	*C*2/m
a (Å)	7.0651(2)	7.3454(16)
b (Å)	9.0096(3)	16.8251(13)
c (Å)	20.2493(5)	23.326(14)
α (°)	78.148(5)	90
β (°)	89.073(6)	91.95(4)
γ (°)	69.912(5)	90
V (Å^3)	1182.65(7)	2881.1(19)
Z	2	4

a) **LT** (20 °C) b) **HT** (177 °C)

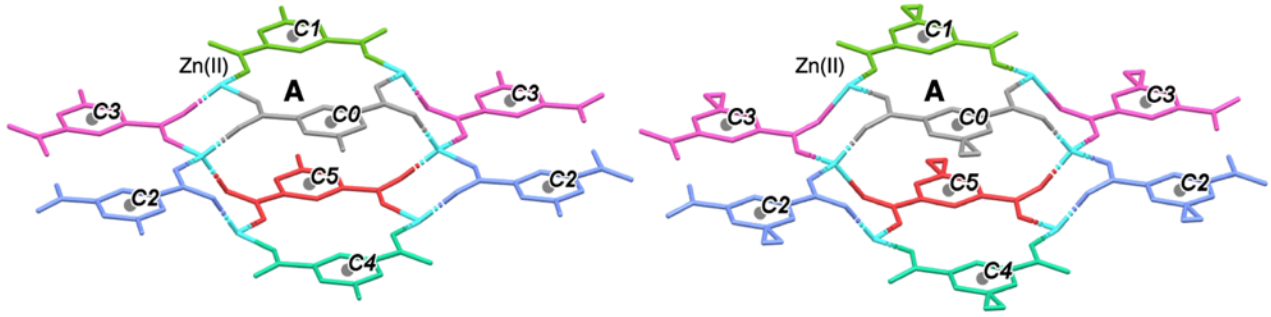

c)

Distance	**LT** (Å)	**HT** (Å)	|Δ| (Å)
C0–C1	8.246	8.195	0.051
C0–C2	9.347	9.179	0.168
C0–C3	10.223	9.949	0.273
C0–C4	7.065	7.345	0.280
C0–C5	4.158	3.985	0.173

Fig. S12 Comparison of the coordination polymer network of **LT** and **HT**. Partial crystal structures of coordination polymer network of a) **LT** (20 °C) and b) **HT** (177 °C). Alkyl chains are omitted for clarity. Ligands locating around the inequivalent relative position to the central one (marked by **A**, coloured by grey) are shown in different colours. *C0*–*C5* represent centroids of each aromatic rings. c) List of the distances among the centroids of aromatic rings in **LT** and **HT**, and their absolute differential values between **LT** and **HT**.

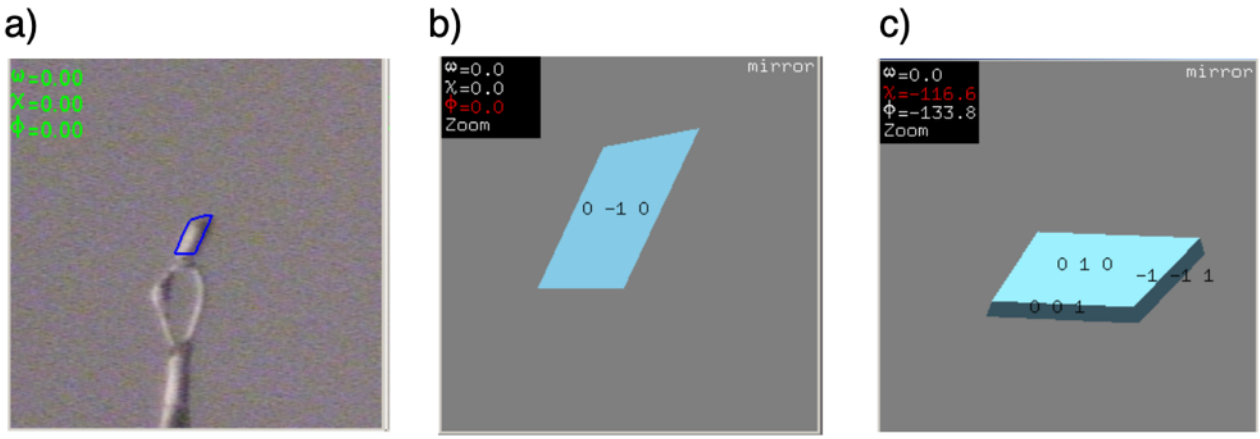

Fig. S13 a) Photograph of a single crystal of **LT**. b-c) Face-indexing graphics of **LT**.

4-6. Visual observation of coordination polymer ZnC16

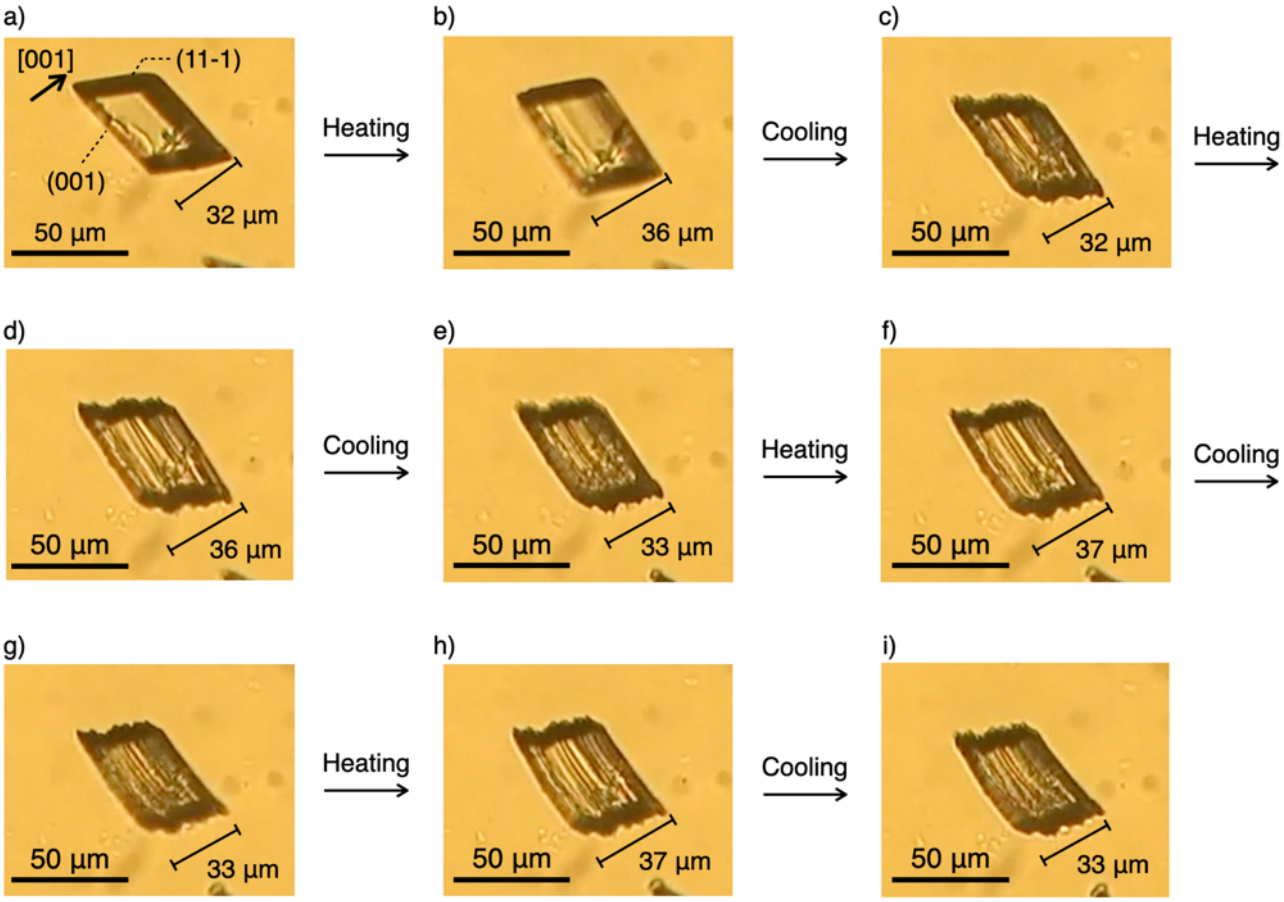

Fig. S14 Photographs showing shape deformation of crystals of Zn**C16** upon repetitive temperature increasing/decreasing cycles within the 140–160 °C window at ca. 20 °C/min (Movie S1). Captions a–i show the sequence of transition. Change in crystal thickness along [001] direction upon temperature cycles is shown in Fig S14, which were estimated by measuring the distances between the opposite (001) axis of the parallelogram shape using microscopic images.

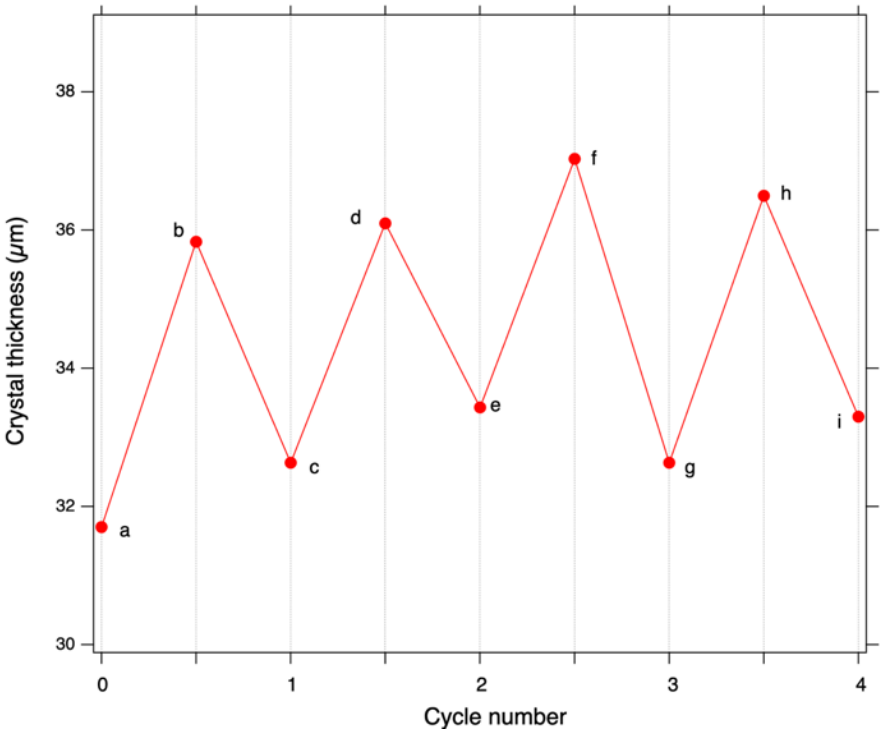

Fig. S15 Change in crystal thickness along [001] direction upon repetitive temperature increasing/decreasing cycles within the 140–160 °C window 20 °C/min. Captions a–i locating next to the circle show the pictures of corresponding crystals in Fig. S13.

4-7. DSC thermograms of coordination polymer ZnC16

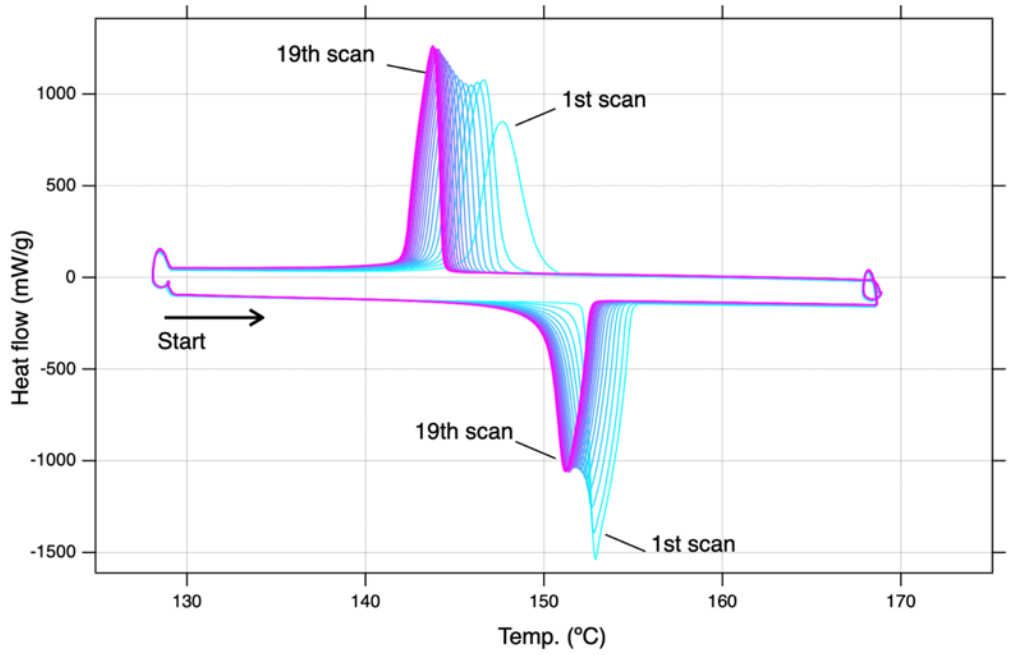

Fig. S16 DSC thermogram of Zn**C16** measured under repetitive temperature increasing/decreasing cycles within the 130–170 °C window. (scan rate 1 °C/min). Thermograms are coloured by cyan (1st scan) to magenta (19th scan) sequentially.

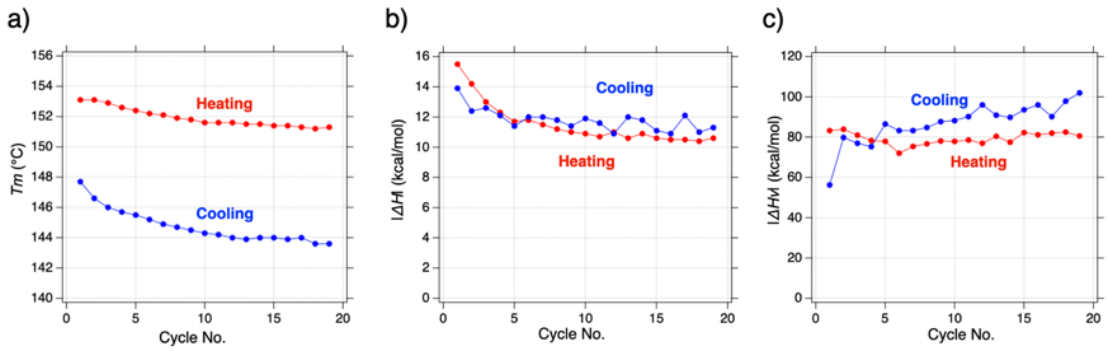

$$C_p(T) = \frac{K(T)\,\Delta Hv\,\Delta H}{(K(T)+1)^2\,RT^2} \qquad \cdots (1)$$

$$K(T) = \exp\left(\frac{-\Delta Hv}{RT}\left(1-\frac{T}{T_m}\right)\right) \qquad \cdots (2)$$

$C_p(T)$: Molar heat capacity

$K(T)$: Equilibrium constant between **LT** and **HT**

Fig. S17 Changes in a) phase transition temperatures (*Tm*), b) absolute values of transition enthalpy (|*ΔH*|), and c) absolute values of van't Hoff enthalpy (|*ΔHv*|) estimated from the curve fitting of the DSC thermograms using eq (1) and eq (2) (Fig. S16). The error values of the curve fitting for *Tm*, |*ΔH*|, and |*ΔHv*| are less than 0.06 °C, 0.5 kcal/mol, and 6.0 kcal/mol respectively.

5. References

1. P. Reb, K. Margarit-Puri, M. Klapper and K. Müllen, *Macrocolecules*, 2000, **33**, 7718–7723.
2. G. M. Sheldrick, *Acta Cryst.*, 2015, **A71**, 3−8.
3. G. M. Sheldrick, *Acta Cryst.*, 2015, **C71**, 3−8.
4. O. V. Dolomanov, L. J. Bourhis, R. J. Gildea, J. A. K. Howard and H. Puschmann, *J. Appl. Cryst.*, 2009, **42**, 339−341.
5. CrysAlisPro, version 1.171.42.56a. Rigaku Corporation, Oxford, UK, 2022.